Thin Solid Films 655 (2018) 1–12

Contents lists available at ScienceDirect

Thin Solid Films

journal homepage: www.elsevier.com/locate/tsf

Enhancing the performance of self-powered ultraviolet photosensor using rapid aqueous chemical-grown aluminum-doped titanium oxide nanorod arrays as electron transport layer

M.M. Yusoff[a,c], M.H. Mamat[a,b,*], A.S. Ismail[a], M.F. Malek[a,b], Z. Khusaimi[b], A.B. Suriani[d], A. Mohamed[d], M.K. Ahmad[e], M. Rusop[a,b]

[a] NANO-ElecTronic Centre (NET), Faculty of Electrical Engineering, Universiti Teknologi MARA (UiTM), 40450 Shah Alam, Selangor, Malaysia
[b] NANO-SciTech Centre (NST), Institute of Science (IOS), Universiti Teknologi MARA (UiTM), 40450 Shah Alam, Selangor, Malaysia
[c] Kulliyyah of Engineering, International Islamic University Malaysia (IIUM), 50728 Kuala Lumpur, Malaysia
[d] Nanotechnology Research Centre, Faculty of Science and Mathematics, Universiti Pendidikan Sultan Idris (UPSI), 35900 Tanjung Malim, Perak, Malaysia
[e] Microelectronic and Nanotechnology – Shamsuddin Research Centre (MiNT-SRC), Faculty of Electrical and Electronic Engineering, Universiti Tun Hussein Onn Malaysia (UTHM), 86400 Batu Pahat, Johor, Malaysia

ARTICLE INFO

Keywords:
Aluminum-doped titanium dioxide
Nanorods
Structural properties
Photoelectrochemical cell
Ultraviolet photosensor

ABSTRACT

Aluminum (Al)-doped titanium dioxide nanorod arrays (ATNs) were grown on fluorine-doped tin oxide-coated glass at different Al atomic concentrations ranging from 1 at.% to 5 at.% in a Schott bottle through single-step aqueous chemical growth for self-powered photoelectrochemical cell-type ultraviolet (UV) photosensor applications. X-ray diffraction patterns showed that the grown ATNs exhibited a crystalline rutile structure. The ATNs showed smaller crystallite size and average nanorod diameter and length compared with the undoped sample. The photocurrent measured from the fabricated UV photosensors improved to some extent with increasing Al-dopant concentration. Samples with 2 at.% Al showed the maximum photocurrent of 108.87 μA/cm^2 at 0 *V* bias under UV irradiation (365 nm, 750 μW/cm^2). The results show that high-performance UV photosensors can be fabricated and enhanced using ATNs easily prepared in a glass container.

1. Introduction

Prolonged exposure to ultraviolet (UV) irradiation may cause various acute and chronic skin disorders and affect vision, bone, neuromuscular, and immune systems. UV monitoring is extremely important and extensively used in several applications, such as missile plume detection, combustion chamber, sensor technology, solar astronomy, and modern generation of fire alarm system [1–4]. The development of UV photosensors using titanium dioxide (TiO_2) materials has been extensively investigated [5–7]. TiO_2 has been widely investigated because of its favorable physical and chemical stability and safety [8]. TiO_2 shows excellent physical, optical, and electrical characteristics and has been proposed for photocatalyst [9,10] and electronic device [11–13] applications. TiO_2 has wide band gap energy of 3.02 eV and 3.20 eV for rutile and anatase, respectively, which facilitates the application of TiO_2 for UV photosensor application [14–16]. Metal doping has been proposed to enhance the properties of TiO_2 [17]. Theoretical and experimental studies have presented that infiltration of metal and non-metal elements can alter the crystallinity and grain size to improve the thermoelectric property in doped TiO_2 [18]. Previous studies also identified the deviations of thermoelectric properties of doped TiO_2 [19,20]. In addition, incorporation of donor energy levels through doping ions can alter the Fermi energy level and band edge shift of the crystalline TiO_2. This process affects thermal and electrical conductivities of the doped materials [21–25].

In a photoelectrochemical cell (PEC)-based UV photosensor system using the TiO_2 electrode, a TiO_2 material with large band gap exhibits high recombination rate of charge carriers. This recombination mostly occurs between TiO_2 and redox couple in an electrolyte on TiO_2/electrolyte interface. Thus, the race between the electron transportation and recombination processes determine the total gain of photocurrent in a self-powered PEC-based system. Several studies have attempted to suppress the recombination by utilizing metal oxide blocking layers [26–30], co-adsorbent [31,32], and $TiCl_4$ treatment [33]. In photocatalyst applications, metal ion doping was reported to impede the recombination of photo-generated electron–hole pairs from TiO_2 by prolonging the lifetime of charge carriers [34–38]. However, only a few studies have reported on the metal-doped layer on the photoelectrode

* Corresponding author.
E-mail address: mhmamat@salam.uitm.edu.my (M.H. Mamat).

https://doi.org/10.1016/j.tsf.2018.03.091
Received 26 December 2017; Received in revised form 26 March 2018; Accepted 30 March 2018
Available online 04 April 2018
0040-6090/

based on TiO2 nanorod arrays in PEC devices particularly related with Al doping [39–41].

In this study, we investigated the effect of aluminum (Al) doping concentrations on the properties of synthesized Al-doped TiO_2 nanorod arrays (ATNs). We performed an improved single-step aqueous chemical growth using a simple modified Schott bottle with cap clamps. Al doping was implemented to elevate the interfacial charge transfer mechanism on the ATNs structure. Most studies on Al-doped TiO_2 have utilized Al atomic content of < 10 at.% [42–44]. However, the optimum doping content will slightly vary between different deposition processes and from application to application. In this study, the influence of Al doping concentration on the structural, optical, and electrical properties of the synthesized ATNs was examined to improve the total gain of photocurrent in the application of PEC-based UV photosensor. To the best of our knowledge, PEC-based UV photosensor using the developed ATNs have not been reported yet. Furthermore, the nature of photogeneration and recombination of the excitonic charge carriers of the developed ATNs in PEC remains unclear. Therefore, this particular study provided an important opportunity to enhance the understanding of the behavior of the developed ATNs based on their structural, optical and electrical properties, as well as subsequent UV sensing performance.

2. Experimental details

2.1. Synthesis of ATNs

Al was used as the dopant for ATNs using a facile single-step aqueous chemical growth at various dopant concentrations. The cleansed fluorine-doped tin oxide (FTO)-coated glass substrates were used as substrate for ATNs growth. First, solutions containing hydrochloric acid (HCl 37%, Merck) and deionized (DI) water in a 1:1 volume ratio were prepared in Schott bottles. After constant stirring for 10 min, 0.07 M tetrabutyl titanate (97%, Sigma-Aldrich) was slowly added into the solutions. Then, aluminum nitrate nonahydrate [$Al(NO_3)_3.9H_2O$, 98% purity; Analar], which act as dopant source, was added into the solutions at different concentrations of 0.05, 0.10, 0.15, 0.20, and 0.25 mM corresponding to approximately 1 at.%, 2 at.%, 3 at.%, 4 at.%, and 5 at.% doping, respectively. The solution without Al dopant was also prepared as a reference. The prepared sample solutions consisting of tetrabutyl titanate, aluminum nitrate nonahydrate, HCl, and DI water, which act as precursor material, dopant source, stabilizer, and solvent, respectively, were stirred vigorously for another 50 min. The cleaned substrates were placed into the solution in Schott bottles with the conductive side of the substrate placed facing upward. Then, the bottles were tightly sealed with a cap and clamped to attain the internal pressure throughout the deposition in an electric oven at 150 °C for 3 h. The schematic for clamped Schott bottle is shown in Fig. 1(a). After the deposition, the samples were rinsed with DI water and blow-dried with nitrogen gas. Finally, the samples were annealed in a furnace at 450 °C for 1 h.

2.2. Device fabrication

The device fabrication of UV photosensor was grounded on the PEC using ATNs at different Al dopant concentrations. The deposited ATNs were designated as the photoanode, and platinized FTO-coated glass substrates were prepared as counter electrode. A spacer was placed between the attachment of the active side of the photoanode and counter electrode. An electrolyte solution of 0.05 M iodine and 0.5 M lithium iodide in acetonitrile solvent was prepared and injected inside the spacer. The filling area of the spacer for UV detection was approximately 1.0 cm^2. Fig. 1(b) displays the diagram of the fabrication of the device.

2.3. Characterization

The deposited ATNs were characterized using X-ray diffraction (XRD, Shimadzu XRD-6000, Cu-Kα radiation, wavelength of 0.154 nm) to investigate the crystallinity of the samples. The XRD measurement was performed in standard θ–2θ Bragg–Brentano geometry configuration using acceleration voltage of 40 kV and applied current of 30 mA in a 2θ range between 20° and 70° with a step size of 0.02° and a step rate of 3°/min. The energy dispersive X-ray (EDX) spectroscopy (Oxford Instruments, X-Max 50 mm^2 detector, operating voltage of 10 kV, working distance of 15.0 mm) and field-emission scanning electron microscopy (FESEM, JEOL JSM6360LA, operating voltage of 5 kV) were conducted to investigate the composition analysis and morphology of the samples, respectively. The samples were also characterized via micro-Raman spectroscopy (Renishaw InVia microRaman System, 514 nm laser) for sample identification and structural and quantitative analysis. The optical properties of the samples were analyzed using ultraviolet-visible-near infrared (UV–vis-NIR) spectrophotometry (Cary 5000). The electrical properties based on the current–voltage (I-V) characteristics of the ATNs were characterized using semiconductor device analyzer system (Keysight B1500A). The optical photoresponse of the fabricated PEC-type UV photosensors based on ATNs at different Al dopant concentrations were investigated using a UV photocurrent measurement system (Keithley 2400) with UV lamp (365 nm, 750 μW/cm^2). Electrochemical impedance spectroscopy (EIS, Solatron-Si1287/Si1260) was also performed to investigate the electrical properties of the fabricated UV photosensors.

3. Results and discussion

Fig. 2(a)–(g) display images of the surface morphology of the synthesized ATNs at different Al dopant concentrations of 0 at.% (undoped), 1 at.%, 2 at.%, 3 at.%, 4 at.%, and 5 at.% samples, respectively. All samples exhibit tetragonal-shaped nanorod structure and are evenly deposited on the substrate. The average diameters of the deposited ATNs 0 at.% (undoped), 1 at.%, 2 at.%, 3 at.%, 4 at.%, and 5 at.% samples are approximately 160, 137, 128, 126, 121, and 119 nm, respectively. These results indicate that the size of the nanorods linearly decreases with increasing Al dopant concentration. The undoped ATNs show the highest average diameter size of nanorods than the other ATNs samples. The analyzed EDX spectra of ATNs at 2 at.% sample is presented in Fig. 2(g). The EDX peaks at 0.452 and 4.058 keV indicate the presence of Ti, while the other peaks at 0.525 keV and 1.486 keV are attributed to O and Al, respectively. Hence, the EDX analysis shows the existence of Ti, O, and Al in the deposited ATNs sample. The results also suggest no other impurities in the synthesized ATNs samples.

Fig. 3(a)–(f) shows the cross-sectional FESEM images of the synthesized ATNs at various Al dopant concentrations at 0 at.% (undoped), 1 at.%, 2 at.%, 3 at.%, 4 at.%, and 5 at.% samples, respectively. The thickness of ATNs decreased slightly with increasing Al dopant concentrations with an average thickness of 2.11, 1.79, 1.71, 1.67, 1.57, and 1.53 μm at Al doping concentrations of 0 at.% (undoped), 1 at.%, 2 at.%, 3 at.%, 4 at.%, and 5 at.% samples, respectively (Table 1). The cross-sectional images also display that the aligned ATNs are perpendicularly grown on the FTO-coated glass substrates, which are expected to enhance electron transportation because of the direct pathway of nanorod structure [45]. The cross-sectional images are also congruent with the top-view FESEM images, which show the decreasing growth of ATNs in correlation with Al dopant concentration. The decrease in the average nanorod diameter and length of ATNs with increasing Al doping content could be due to the suppression of particle growth by the addition of dopant into the parent TiO_2 crystalline structure [46].

Fig. 4 displays the XRD results of the deposited ATNs. The diffraction peaks detected at (110), (101), (111), (211), and (002) planes designate the tetragonal-faceted nanorods of rutile structure TiO_2 (JCPDS No. 01-072-1148), and no peaks show anatase and brookite

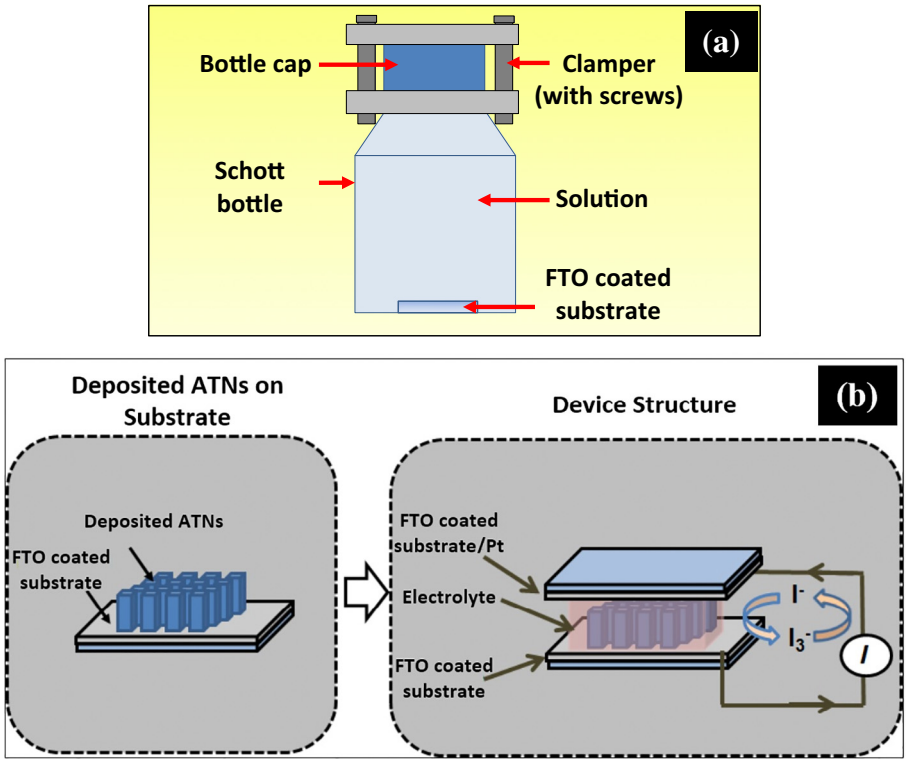

Fig. 1. (a) Schematic of clamped Schott bottle for ATNs deposition. (b) Schematic of the ATNs and device structure of the PEC-based ultraviolet photosensor.

structures. The peaks that represent the Al and secondary phases and clusters, such as Al_2O_3 crystal structure, are also not observed, which indicates that Al is homogenously doped and dissolved into the parent TiO_2 rutile structure [47,48], as confirmed by the EDX results. Previous studies highlighted that Al_2O_3 could be produced to change some properties of nanostructured TiO_2 when Al is doped to some extent [49,50]. Thus, the absence of Al_2O_3 peaks in some results could be attributed to the formation of a new spinel phase structure of $TiAl_2O_5$ [46], which is too small to be detected by XRD measurement. Meanwhile, SnO_2 peaks representing the FTO-coated glass substrate are marked by stars in Fig. 4. The vertically growth ATNs along the *c*-axis is represented by the (002) peak, and the intensity of the peaks corresponds to the number of growth [51,52], which is inversely proportional to the Al dopant concentrations. This result indicates that the Al atoms are effectively incorporated into the TiO_2 lattice. The widening of the peak could also be observed as Al concentration increased. These results suggest that the parent structure of TiO_2 could have been distorted, with increasing of Al dopant concentrations [53–55]. Ti^{4+} ion with large radius (0.068 nm) are substituted by Al^{3+} ion with smaller radius (0.051 nm) in the rutile ATNs. However, substitution leads to the formation of tension in the crystal structure, and this process could be attributed to dissimilar oxidation state, ionic radius, and electronegativity [55]. The analyzed data also show that the diffraction peak of (002) slightly shifts to higher angle values. Zhang et al. explained that the shift of diffraction peaks depends on the ionic radius of the incorporated metal ion into TiO_2 crystal lattice [56]. The incorporation of metal ion with smaller radius shifts the diffraction peak to higher angle, while metal ion with larger radius shifts the diffraction peak to lower angle. The ATNs are also represented by (101) peak, which results from the diffraction of the X-ray at the side surface of the ATNs [51,57]. The growth rate of ATNs from the unit cell of TiO_6 octahedron depends on the amount of corners and edges available from the octahedral formed and Al dopant concentration in the solution during growth. The growth of rutile ATNs is congruent to the XRD peaks also in conjunction with the sequence of (110) < (100) < (101) < (001) [58]. The sequence is similarly in agreement with the rutile ATNs which are represented by (101) and (001) directions and evenly deposited on the whole surface area of the substrate for all ATNs samples. Moreover, the growth of ATNs on the FTO-coated glass substrate is also due to the fact that the FTO retains to some extent the tetragonal structure of rutile TiO_2 with small lattice mismatch value of FTO ($a = b = 0.4687$) and rutile TiO_2 ($a = b = 0.4594$), respectively at 2 at.% [59], regardless of the addition of Al dopant. The noise level in XRD data found to be decreased, when the Al concentration is increased from 0 at.% (undoped) to 3 at.%. However, the noise increased when the Al-doping is further increased to 5 at.%. According to Ishii et al., the Al doping promotes the formation of the rutile phase of TiO_2. Considering that the XRD measurement parameters are equal for all samples, we believe that the Al doping improves the rutile phase of TiO_2 up to 3 at.% of the Al atomic concentration. This condition might reduce the noise level in XRD data as the phase of rutile TiO_2 is enhanced. However, the rutile phase of TiO_2 might be degraded with the further increased of Al atomic concentration at 4 at.% and above, which possibly increase the noise level in the XRD data.

The average crystallite sizes $D_{(002)}$ of the undoped and ATNs are calculated using Scherrer's equation, as written in the following equation:

$$D_{(002)} = \frac{0.94\lambda}{\beta \cos\theta} \quad (1)$$

where λ is the wavelength of the X-ray used (0.154 nm), β is the full width at half maximum (FWHM) of the represented (002) plane, and θ is the peak position of the X-ray used. The calculated values for the equations are presented in Table 2. The average crystallite size of the undoped sample was 30.0 nm, and ATNs were in the range of 28.7–27.6 nm for 1 at.%–5 at.% samples. These results show that the crystallite size decreases to some extent with Al doping and increasing Al dopant concentrations. The undoped sample shows the largest value compared with all ATNs samples. These results may partly be explained by the difference between the ionic radii of Ti^{4+} ion (0.068 nm) and

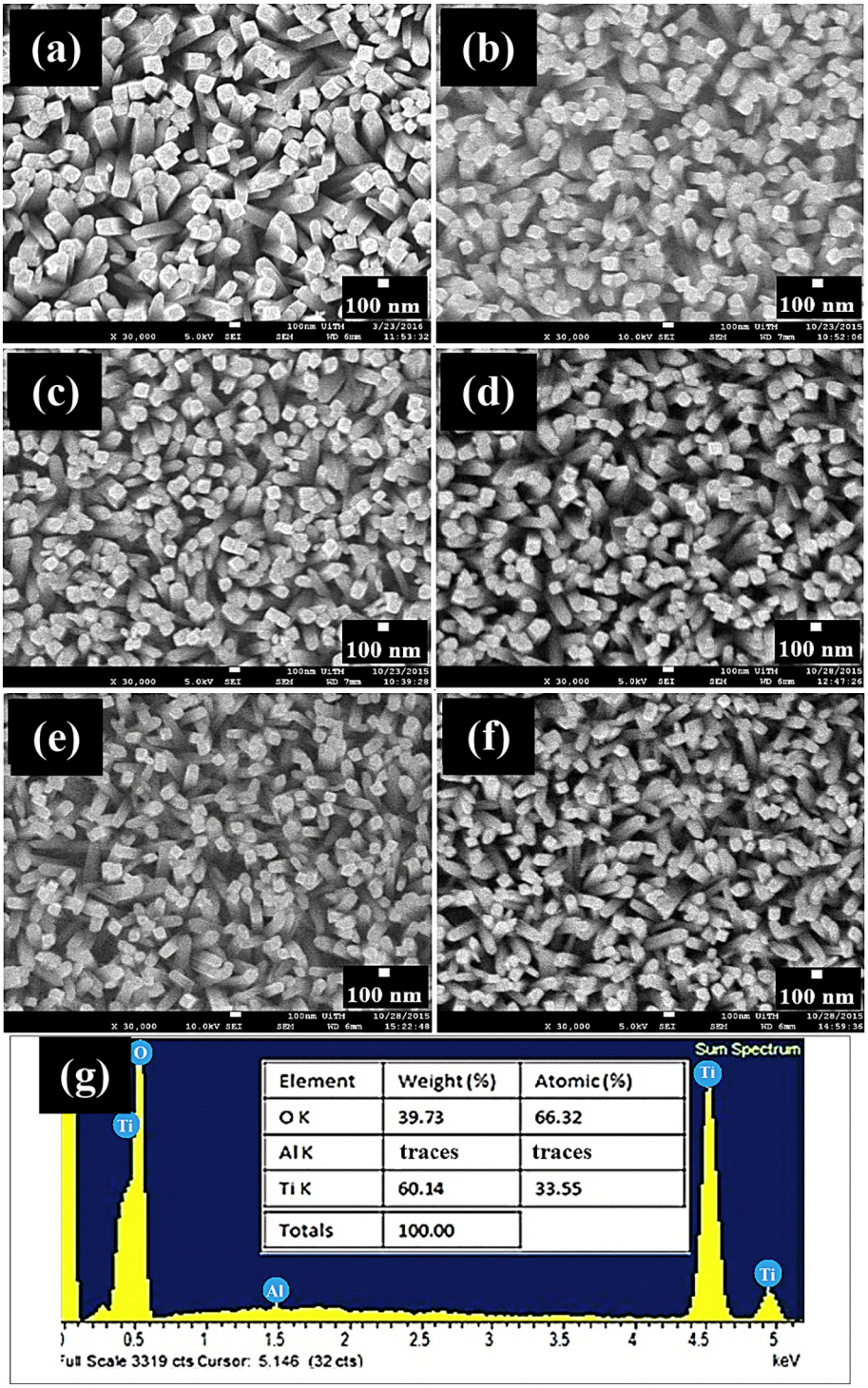

Fig. 2. FESEM surface morphology for (a) undoped TiO_2, (b) 1 at.%, (c) 2 at.%, (d) 3 at.%, (e) 4 at.%, and (f) 5 at.% ATNs samples, respectively, and EDX spectrum of (g) 2 at.% ATNs sample.

Al^{3+} ion (0.051 nm) [55]. The decrease in crystallite size is likely to reduce the size of tetragonal-faceted nanorods of ATNs.

The XRD data of synthesized ATNs at various Al dopant concentrations were also utilized to calculate the lattice parameters of *a*- and *c*-axes based on the (101) and (002) planes of the XRD patterns as follows [60–62]:

$$\frac{1}{d^2} = \frac{h^2 + k^2}{a^2} + \frac{l^2}{c^2} \tag{2}$$

where d is the gap between the planes, which is based on 2θ from Bragg's Law [Eq. (3)]; and h, k, and l are the Miller indices.

$$d = \frac{\lambda}{2\sin\theta} \tag{3}$$

The calculated lattice parameters from the XRD data in Table 2 reveal that a steady decrease from 0.4653 nm to 0.4624 nm and 0.2976 nm to 0.2969 nm for *a*- and *c*-axes of 0 at.% (undoped) and doped samples, respectively. The results indicate negative correlation between the Al dopant concentration of the sol-gel during growth and the lattice parameters for both *a*- and *c*-axes. The decrease in lattice

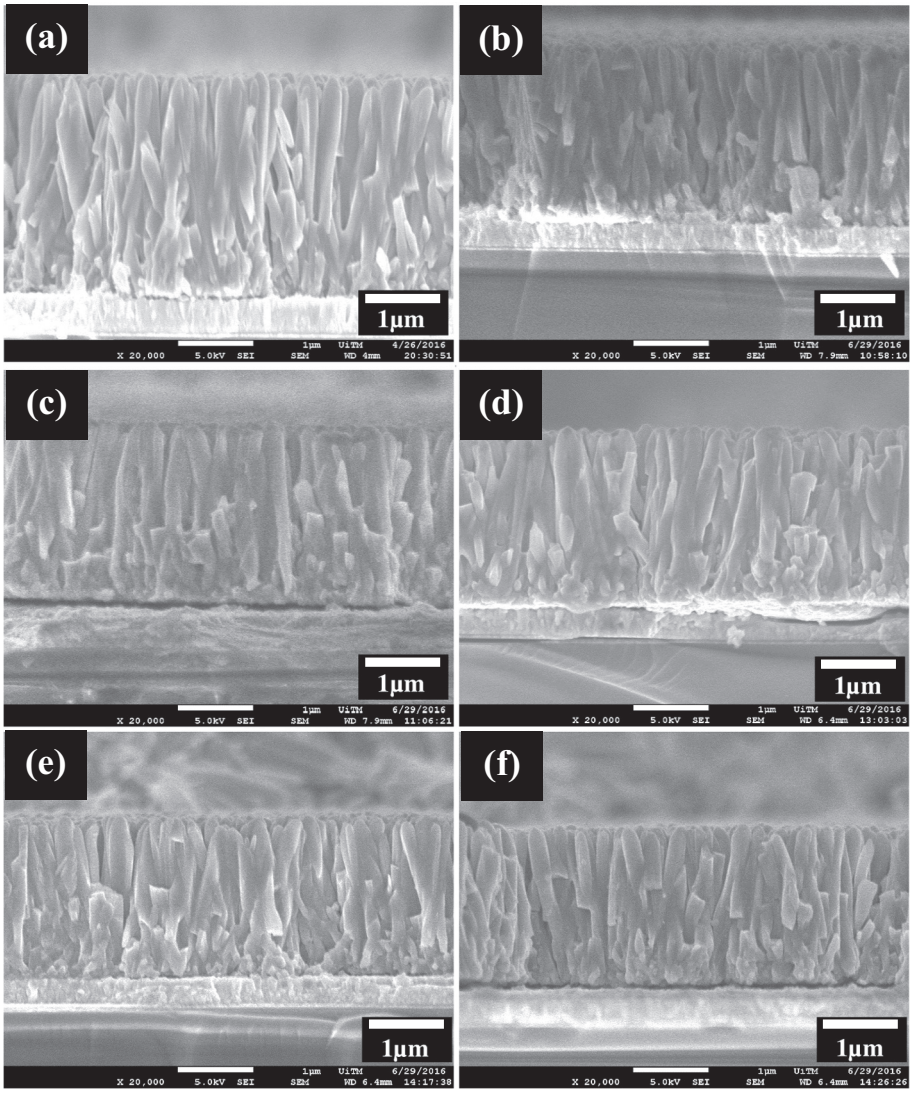

Fig. 3. Cross-section images of (a) undoped TiO_2, (b) 1 at.%, (c) 2 at.%, (d) 3 at.%, (e) 4 at.%, and (f) 5 at.% of ATNs samples.

Table 1
Average diameter, thickness, and optical band gap energy of ATNs at various Al dopant concentrations.

Samples (Al-doped)	TNAs average diameter (nm)	TNAs average thickness (μm)	Optical band gap energy (eV)
Undoped	160	2.11	3.02
1 at.%	137	1.79	2.99
2 at.%	128	1.71	2.97
3 at.%	126	1.67	2.96
4 at.%	121	1.57	2.94
5 at.%	119	1.53	2.89

parameters is due to the substitution of larger Ti ion by smaller Al ion. This phenomenon decreases the particle size as discussed in previous reports [46,63]. Thus, the incorporation of Al ions into the TiO_2 crystalline structure is through the substitution of Ti ions, and not by the diffusion into the interstitial void of the TiO_2 lattice structure [56]. After analyzing the measured strain (ζ_c) along the *c*-axis in rutile ATNs, the correlation between one of the axes and strain is determined from the calculated lattice parameters with Eq. (4) as follows [61,64]:

$$\zeta_c = \frac{c - c_o}{c_o} \times 100\% \quad (4)$$

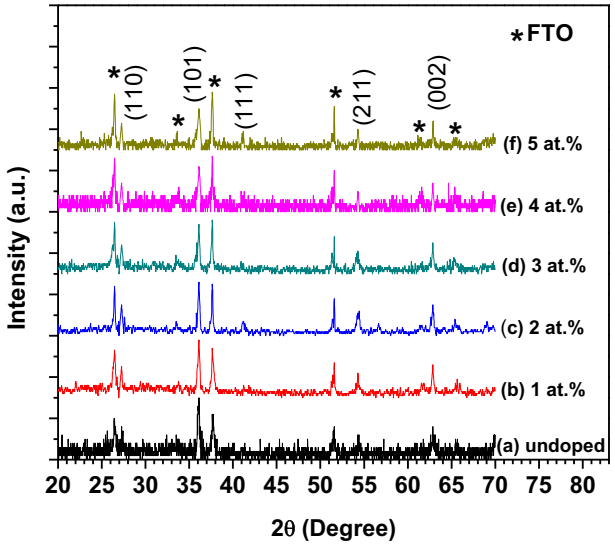

Fig. 4. XRD patterns of (a) undoped TiO_2, (b) 1 at.%, (c) 2 at.%, (d) 3 at.%, (e) 4 at.%, and (f) 5 at.% ATNs samples.

Table 2
Relative peak intensity, crystallite size, strain, lattice mismatch, and lattice parameters of the ATNs samples.

Samples	Relative peak intensity (TNAs)	Crystallite size (nm)	Strain of *c*-axis (%)	Lattice mismatch of *d* (%)	Lattice parameters		
					a (nm)	*c* (nm)	*c*/*a*
Undoped	0.830	30.0	0.608	0.561	0.4653	0.2976	0.640
1 at.%	0.821	28.7	0.486	0.439	0.4640	0.2972	0.641
2 at.%	0.819	28.4	0.456	0.409	0.4635	0.2971	0.641
3 at.%	0.818	28.2	0.441	0.394	0.4633	0.2971	0.641
4 at.%	0.815	27.8	0.403	0.356	0.4627	0.2970	0.642
5 at.%	0.814	27.6	0.387	0.340	0.4624	0.2969	0.642

where c and c_o are the lattice parameters of the strained ATNs attained from the XRD data and the standard data of the unstrained bulk TiO_2, respectively. Table 2 shows that the overall tensile strain initially decreases from 0.608% to 0.387% with increasing Al dopant concentration. This phenomenon is attribution to the slight formation of compressive strain at the dislocation side by the substitution of Ti^{4+} ions by smaller ionic radius of Al^{3+} ions. Initially, the growth on the undoped sample generated high tensile strain as the nucleation of nanoparticles impinge one another, and the nanoparticles coalesce before the thickening of the film [65]. In addition, most defects, such as dislocations, broken bonds, and substoichiometric composition, on the crystal structure occur at grain boundaries during synthesis [66]. The high strain formation in the deposited undoped films might be attributed to all defects. However, the tensile strain reduction in ATNs is due to the shorter distance of Al−O bond compared with the Ti−O bond. This characteristic leads to compression in the lattice constants and reduction in grain size as shown by previous studies [46,67]. The net strain is also attributed to the existence of total distortion in a unit cell structure because of the peculiarities of interplanar distance (d) values of the deposited ATNs samples compared with bulk TiO_2. The distortion was analyzed from the lattice mismatch (Δd) in accordance with the following equation [68]:

$$\Delta d = \frac{d - d_o}{d_o} \times 100\% \tag{5}$$

where d and d_o are the interplanar distances of rutile ATNs from the XRD data and the interplanar distance of standard TiO_2, respectively. The lattice mismatch analysis in Table 2 shows that the net lattice mismatch decreases from 0.561% to 0.340% with increasing Al dopant concentration. The occurrence of strain and lattice mismatch caused by the distortion of lattice parameters from its standard value could be due to the presence of microstress and macrostress from the widening of the diffraction peaks. The stresses generally result from the defects in the deposited films and may form implications on its unit cell structure to diverge from its ideal stoichiometry. Macrostress expands the average crystallite size, while microstress produces the widening of the diffraction peak [61,62].

The XRD data of synthesized ATNs at various Al dopant concentrations are utilized to estimate the relative peak intensity orientation $P_{(hkl)}$ of the nanorod growth of ATNs along the (002) plane. This characteristic substantially influences the improvement in charge transportation [69,70], according to Eq. (6) [71]:

$$P_{(\mathrm{hkl})} = \frac{I_{(\mathrm{hkl})}}{\sum I_{(\mathrm{hkl})}} \tag{6}$$

where $I_{(hkl)}$ is the peak intensity of (hkl), and $\Sigma\, I_{(hkl)}$ is the overall intensities of all diffraction peaks of the deposited ATNs on the substrate. The relative peak intensity along the (002) plane slightly decreases with increasing Al dopant concentrations from 0.830 for the undoped sample to 0.814 for the doped samples. The relationship may partly be explained by the decrease in thickness with increasing Al dopant concentrations. The XRD results of the deposited ATNs are in accordance with the growing mechanisms through the nucleation and crystallization involved in aqueous chemical growth. Throughout crystallization, subsequent increase in nucleation number per unit area supports the growth of crystal nucleus, which is important in the increase in crystallite size [72,73]. However, the decrease in crystallite size suggests the incorporation of Al ions, which is smaller in atomic size, into the rutile TiO_2 crystal structure through the substitution of Ti ions in the crystal lattice [46]. The substitution may also break the continuity of the crystal structure and therefore leads to the highest crystallite size for the undoped TiO_2 [55]. Thus, nucleation during the growth of crystal nucleus may be assumed to be the same to some extent for all ATNs samples because of the constant values of other parameters. In addition, reduction in the average crystallite size may be explained by the decrease in lattice parameters of a- and c-axes as calculated based on the XRD pattern. The peculiarity of lattice parameters indicates the defect formation of oxygen vacancy [60] and substitution of Ti by Al contents in the deposited samples. Moreover, the XRD result of (002) peak for all samples shows the shift of the peak to some extent toward the standard value of TiO_2 peak with increasing Al dopant concentrations. This phenomenon demonstrates the overall relaxation of crystal lattice structure, consequently minimizing surface energy and total stress of the deposited film [64], as shown in our previous strain analysis.

Raman spectroscopy is performed to confirm the phase, crystallinity, and defects of the synthesized ATNs at various Al dopant concentrations (Fig. 5). All samples show discrete Raman bands of the rutile TiO_2 at 143, 235, 447, and 612 cm^{-1}, representing B_{1g}, two-phonon bands (marked as *), E_g, and A_{1g}, respectively [74,75]. Distinct peak is detected at E_g and A_{1g} as well as the two-phonon bands, while small B_{1g} peak is observed for all samples. No peaks of anatase and brookite are observed, which are congruent with the XRD result. Table 3 displays the frequency shift of Raman bands for all deposited

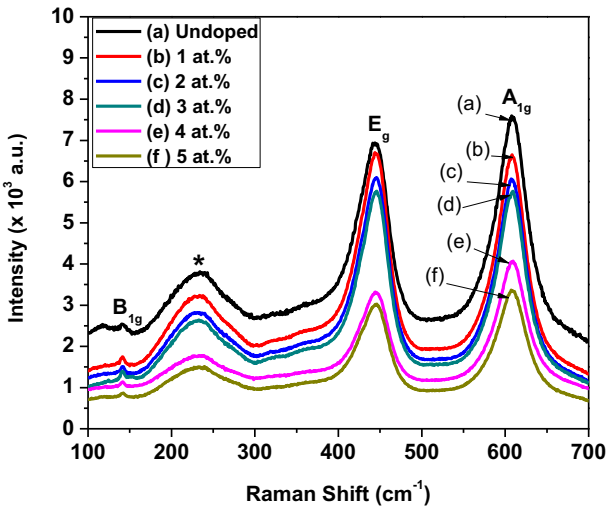

Fig. 5. Raman spectra of undoped TiO_2 and ATNs samples with various Al contents.

Table 3
Raman bands of prepared ATNs grown at various Al dopant concentrations.

Samples	Raman bands of prepared rutile TNAs			
	B_{1g} (cm^{-1})	Two-phonon bands (*) (cm^{-1})	E_g (cm^{-1})	A_{1g} (cm^{-1})
Undoped	141.7	233.5	445.6	610.5
1 at.%	141.7	233.5	446.1	610.5
2 at.%	142.3	234.0	446.1	610.5
3 at.%	142.3	234.0	446.1	611.6
4 at.%	142.9	234.0	446.7	611.6
5 at.%	142.9	234.5	446.7	611.6

samples. All samples including the highest intensity of E_g and A_{1g} mode are red-shifted for all frequency shifts. The red shift of E_g and A_{1g} modes, which are shifted toward lower wavenumbers, may be partially described by phonon confinement effect and oxygen vacancy defects [76,77] of rutile TiO_2 from asymmetrically broadened Raman lines. In addition, the frequency shift could also be attributed to the stress induced by the surface stress [78], which is in agreement with our XRD analysis at various Al dopant concentrations. However, the frequency shift increases to some extent toward higher wavenumbers from the undoped value with increasing amount of Al dopant. This characteristic is attributed to the substitution of Ti by Al, which alters the ionic radii, oxidation states, and electronegativity [55].

Oxygen vacancies are produced by the difference in the oxidation states of Ti and Al ions to preserve the local charge neutrality and phase shifts [55,79]. Therefore, the existence of oxygen vacancies from the doping material affects the Raman shifts and intensity of the peaks on the Raman spectra. The sensitivity of Raman spectroscopy on the TiO_2 crystalline structure is also dependent on phonon vibration and polarizability of O^{2-} in the Ti—O bond of the basic octahedral [80]. Thus, the existence of oxygen vacancies by Al doping affects the strength of Raman signal at the vicinity of the defect vacancies, resulting in the overall shift to higher wavenumber [79,81,82]. The results further confirmed the association between frequency red shift and average crystallite size [83] as measured from our XRD data. The highest intensity of Raman spectra represents the concentration of the sample or number of molecules in the sample. Fig. 5 shows that the intensity decreases with increasing Al dopant concentrations. This result may have been caused by the penetration depth of the excitation incident light into the sample. The value of this depth is low in the number of molecules in correlation with Al dopant concentration to some extent. Thus, the inelastic scattered light excited from the sample increases.

UV–vis transmittance spectra of ATNs at room temperature for the undoped and doped samples in the wavelength range from approximately 350 nm to 500 nm as shown in Fig. 6. All rutile ATNs samples transmit and absorb light at nearly 410 nm wavelength as shown by the increasing slopes. This result is comparable to the 3.02 eV band gap energy of rutile TiO_2, because of the excitonic electrons in the conduction bands [84]. The lowest transmittance was at the smallest Al dopant concentration because of the decrease in thickness and size of the ATNs, which is consistent with the FESEM results. The decrease in thickness and size of ATNs may also have reduced the light scattering effect in between the grain boundaries. This phenomenon increases the transmittance of the deposited ATNs. The UV–vis spectral data are used to obtain the absorption coefficient via Lambert's Law based on Eq. (7) as follows [85]:

$$\alpha = \frac{1}{t}\ln\left(\frac{1}{T}\right) \tag{7}$$

where t is the thickness of the film, and T is the transmittance of the film.

The absorption coefficients of ATNs at various Al dopant concentrations are displayed in Fig. 7. The plotted graph shows a sturdy increase in the absorption coefficient with increasing Al dopant

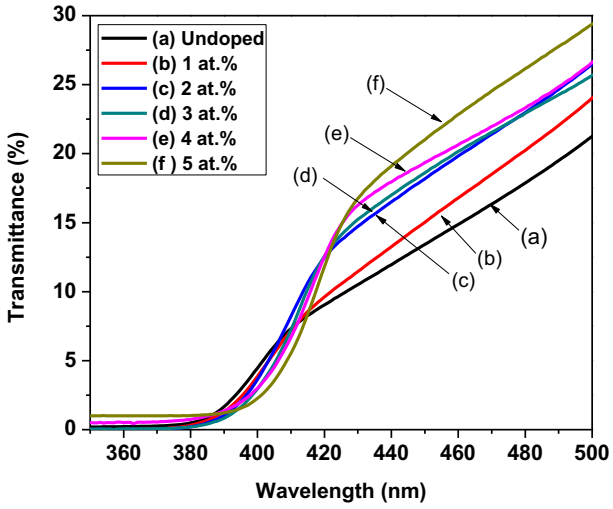

Fig. 6. UV–vis transmittance spectra of undoped TiO_2 and ATNs film.

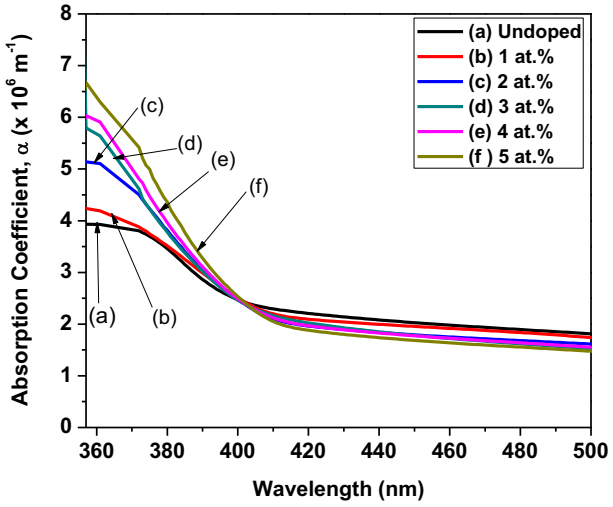

Fig. 7. Absorption coefficient α of undoped TiO_2 and ATNs films as a function of wavelength.

concentration. In addition, absorption edges can be observed in the UV region (< 400 nm) for all samples. The absorption edges also slightly shifted to higher wavelength with increasing Al dopant concentration. This result is consistent with the defect formation as discussed in the XRD analysis previously.

The band gap energies E_g of the synthesized and deposited samples are also calculated based on the Tauc's plot in the measured range using Eq. (8) as follows [86–88]:

$$(\alpha h\nu)^2 = A(\mathrm{hv} - \mathrm{E_g}) \tag{8}$$

where α is the absorption coefficient, $h\nu$ is the photon energy, A is an absorption constant, and E_g is the band gap. The band gap energy E_g was extrapolated from the linear line on the plotted graph in Fig. 8 of $(\alpha h\nu)^2$ versus $h\nu$ curve for the deposited ATNs samples. The band gap of each deposited sample at various Al dopant concentrations are displayed in Table 1. The altered values in the band edge region on the plotted graph exhibit a linear curve, inferring the direct transition of the deposited rutile ATNs [89,90]. The band gap is reduced from 3.02 eV to 2.89 eV with increasing Al dopant concentration. The decrease in band gap energy also further supports the shift in the absorption edges in the absorption coefficient diagram toward the higher value of wavelength to some extent with increasing Al dopant concentrations.

The electrical properties of the fabricated UV photosensors based on

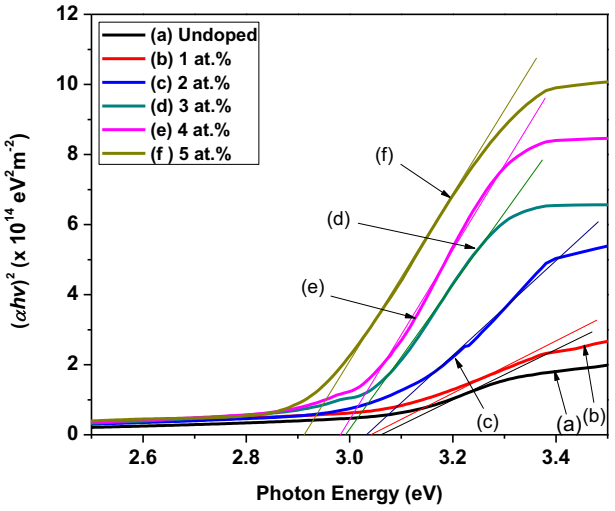

Fig. 8. Extrapolation of the optical band gap energy E_g of undoped TiO_2 and ATNs films using Tauc's plot.

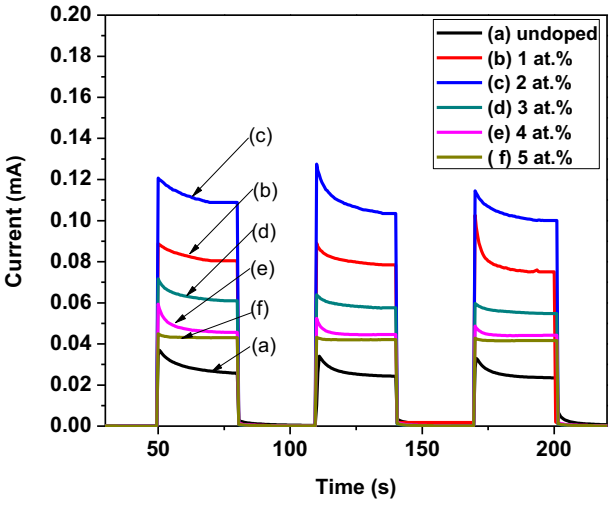

Fig. 9. Photocurrent response under UV irradiation (365 nm) of the fabricated UV photosensors of the deposited undoped TiO_2 and ATNs samples.

PEC structure using the deposited ATNs are measured through the generated photocurrent under "on" and "off" states for repetitive switching cycles of UV irradiation (365 nm) at 0 V bias for the undoped and doped ATNs samples. The measured photocurrent is displayed in Fig. 9. The photocurrent for all samples increases and decreases rapidly during the "on" and "off" states, respectively. The constant result of photocurrent under repetitive switching cycles in all samples also indicates that the fabricated UV photosensor using the deposited ATNs remarkably respond to the changes in the UV signal. The UV irradiation with energy higher than the band gap energy of the synthesized ATNs can excite the electrons from the valence band to the conducting band and leave holes in the valence band to generate photocurrent.

Thus, such *n*-type TiO_2 is likely to detach from the Ti^{3+} and oxygen vacancies (V_O) when exposed to UV irradiation [91,92]. The detachment could be described by the following reaction [93]:

$$Ti^{4+}O_2^{2-} \rightarrow Ti_{1-2x}^{4+}Ti_{2x}^{3+}O_{2-x}^{2-} + xV_O + 0.5xO_2 \quad (9)$$

When exposed to UV irradiation, excitonic charge carriers of electron and hole pairs are generated based on the following equation:

$$hv \rightarrow e^- + h^+ \quad (10)$$

where hv is the photon energy of UV irradiation, and e^- and h^+ are the excitonic electron and hole, respectively. The oxygen vacancies are then formed in the crystalline structure through the discharge of O^{2-}. In addition, the substitution of Ti^{4+} by Al^{3+} in the rutile TiO_2 crystalline structure to form oxygen vacancies could be based on the following equation [93]:

$$(1 - 2x)TiO_2 + xAl_2O_3 \rightarrow Ti_{1-2x}Al_{2x}O_{2x} + xV_O \quad (11)$$

The excited electrons under UV irradiation are transported through the nanorods to the conductive side of FTO-coated glass substrate and produce photocurrent, while the remaining holes are transported toward the ATNs/electrolyte interface. The excited electrons produce external current and transported to the counter electrode to recombine with the reduced electrolyte. Meanwhile, the photo-generated holes at the interface of ATNs/electrolyte diffuse into the electrolyte as part of the internal circuit as described in the following equation [6]:

$$3I^- + 2h^+ \rightarrow I_3^- \quad (12)$$

$$I_3^- + 2e^- \rightarrow 3I^- \quad (13)$$

The excitonic electrons transported to the surface of counter electrode will recover the triiodide (I_3^-) into iodide (I^-) to replete the closed loop circuit. Thus, the oxidized ATNs during irradiation will reduce back into its original state through the redox reaction in the electrolyte. In addition, the redox species in the electrolyte complete the closed loop cycle of charge carriers without any chemical alterations [94,95].

The transportation of excitonic charge carriers under UV irradiation mainly determines the performance of the fabricated UV photosensor using the deposited ATNs. The rise of electron mobility increases the photocurrent in an "on" state and instantly yields to its initial dark current during an "off" state [11,96]. The performance through the generated photocurrent of the fabricated UV photosensors using the deposited ATNs at various Al dopant concentrations is summarized in Table 4. The fabricated UV photosensor from undoped sample displays the photocurrent of 26.31 μA. The generated photocurrent increases to 80.46 and 108.87 μA, with addition of Al dopant concentration for 1 at. % and 2 at.% samples, respectively. FESEM results show that the diameter and length of nanorods decrease with increasing Al dopant concentration for ATNs samples. Therefore, the Al dopant concentration in ATNs plays an important role in determining the interaction between the semiconducting material and the electrolyte. However, the generated photocurrent decreases to 61.01, 45.67, and 43.01 μA with increasing Al dopant concentration of 3 at.%, 4 at.%, and 5 at.%, respectively. This result shows that the photocurrent of the fabricated UV photosensor did not increase as postulated with increasing Al dopant concentration from 3 at.%. Okuya et al. described that the possible decrease in photocurrent was to some extent due to the decrease in crystallinity with increasing Al dopant concentration [97]. This result differs from the findings presented in the current considering that crystallinity slightly changes as shown by the XRD result. Therefore, this finding is likely related to the increase in the recombination of excitonic charge carriers. The photocurrent decay occurs upon UV irradiation in all samples. At the beginning of the "on" position, a photocurrent spike is observed and gradually decreases until it reaches a stable state. The photocurrent decay could be attributed to the

Table 4
Electrical properties of the synthesized ATNs samples.

Samples	Photocurrent, I ($\mu A \cdot cm^{-2}$)	Resistivity, ρ (MΩ·cm)	Conductivity, σ ($nS \cdot cm^{-1}$)
Undoped	26.31	174.26	0.57
1 at.%	80.46	156.68	0.64
2 at.%	108.87	152.28	0.66
3 at.%	61.01	150.08	0.67
4 at.%	45.67	144.59	0.69
5 at.%	43.01	142.39	0.70

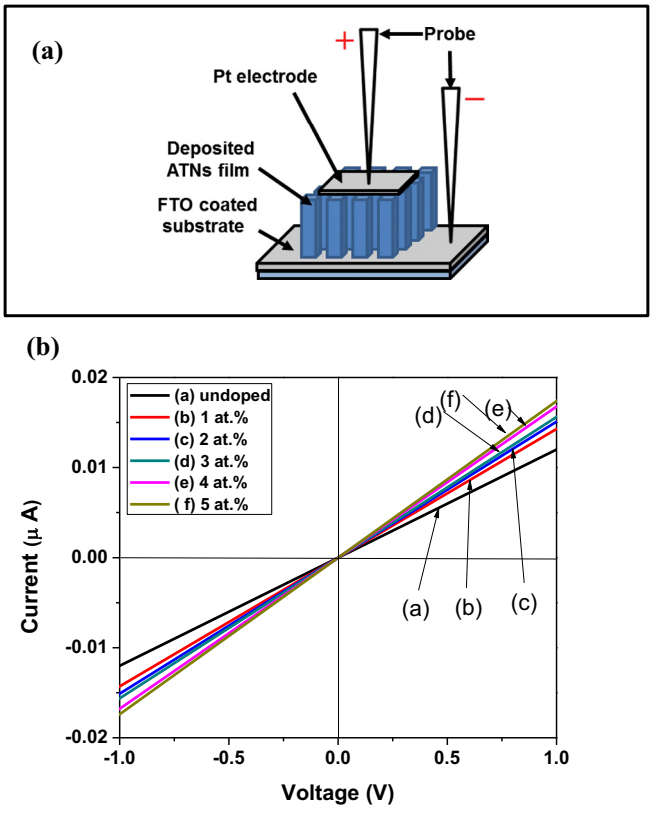

Fig. 10. (a) Schematic for *I–V* measurement and (b) *I–V* characteristic of undoped TiO_2 and ATNs samples at linear region (−1.0 V–1.0 V).

abundant generation of charge carriers caused by the accumulation of electrons in the bulk or holes on the surface which immediately recombined after generation [98]. The result is also likely related to the deficiency in electron transportation in the fabricated photoanode. However, the decay in our photocurrent results is insignificant because of the difference between the maximum spike and stable photocurrent values and comparatively higher than the photocurrent value at "off" state.

The I-V measurement of synthesized ATNs for the undoped and doped samples was performed via FTO/ATNs/Pt MSM structure as displayed in Fig. 10. The schematic of I–V measurement is shown in Fig. 10(a) and (b) shows the results of the I–V measurement of the ATNs samples in the range of −1.0 V to 1.0 V at room temperature. The linear part, which exhibits an Ohmic characteristic at approximately below 1.0 V, is utilized to measure the electrical properties of the deposited ATNs samples. The measured electrical properties are displayed in Table 4. Table 4 illustrates that the resistivity decreases from 174.26 MΩ·cm to 142.39 MΩ·cm, while the conductivity increases from 0.57 nS/cm to 0.70 nS/cm for undoped to 5 at.% samples, respectively. The results of this study show a positive correlation between the conductivity and Al dopant concentration. This result is likely to be related to the formation of high-conductivity phase of $Al_xTi_{1-x}O_2$ in the TiO_2 crystalline structure [46]. Another possible explanation for this phenomenon is the fact that the substitution of Ti^{4+} by Al^{3+} also increases the oxygen vacancies in the rutile TiO_2 structure [99]. Therefore, the conductivity of the deposited ATNs is increased under the electrical potential values.

The performance of UV photosensor based on generated photocurrent is basically subjected to light-trapping and hole-trapping mechanisms and the existence of chemisorbed oxygen molecules of the electrolyte at the interface [100,101]. In the dark state without the UV irradiation, the ATNs/electrolyte interface produces a high-resistance carrier-depletion region in attribution to the presence of free electrons

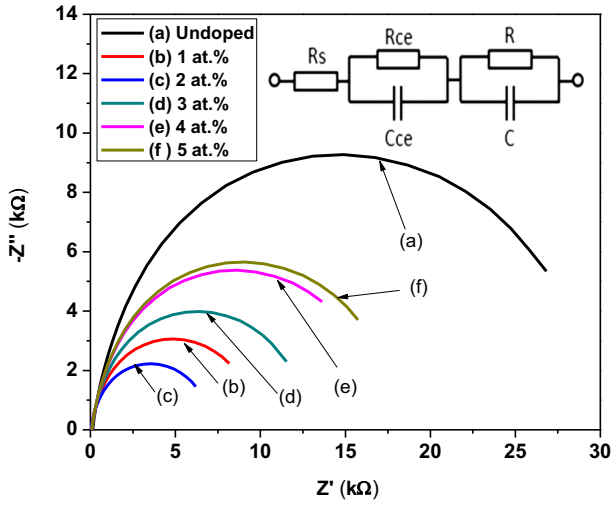

Fig. 11. EIS Nyquist plots of the fabricated UV photosensor of the deposited undoped TiO_2 and ATNs samples under UV irradiation (365 nm, 750 μW/cm^2).

in the n-type ATNs which captured by the absorbed oxygen molecules in the electrolyte [102]. The oxygen from the interface of this region is then desorbed under the UV irradiation which possesses energy exceeding the energy gap of the deposited ATNs of the fabricated UV photosensor. Overall, the performance of the fabricated UV photosensor is determined by the light-trapping and hole-trapping mechanisms, and mostly correlated with the active interface area. In addition, the electrical response of the nanoscale materials is also determined by the hole-trapping mechanism of the absorbed and desorbed oxygen [101,102]. The surface area of the nanoscale materials is also highly reactive to the surrounding. By contrast, the fabricated UV photosensor has minimal influence from the surrounding in attribution to the distinctive structure of PEC.

The recombination process at the surface of deposited ATNs and the transportation of charge carriers of the fabricated UV photosensor are examined using EIS. The analysis was performed under UV irradiation (365 nm, 750 μW/cm^2) in the frequency range from 0.1 Hz to 10^4 Hz. Fig. 11 displays the Nyquist plots of fabricated UV photosensor using the deposited ATNs for the undoped and doped samples. The inset of Fig. 11 shows the circuit model to represent the following: the impedance states, which resembles to the charge transfer resistance at ATNs/electrolyte and capacitance of ATNs (R and C) at intermediate frequency; and charge transfer resistance and Helmholtz capacitance at the electrolyte/FTO (R_{CE} and C_{CE}) interface at high frequency. The series of external resistance at low frequency is represented by R_s [84,103,104]. The performance of the fabricated UV photosensor is mainly determined by the semicircles in the plotted graph, which is represented by the R at intermediate frequency. R_{CE} and R_s are relatively small and nonsignificant compared with R in the plotted graph. Thus, the charge transfer at the ATNs/electrolyte interface is the central aspect for the U*V* sensing of the developed device. Table 5 presents the

Table 5
Simulative value of resistances (R_s, R_{CE}, and R) from electrochemical impedance spectra analyzed by equivalent circuit, and lifetime of electrons (τ) of ATNs samples in PEC cell structure.

Samples	R_s (Ω)	R_{CE} (Ω)	R (kΩ)	τ (ms)
Undoped	17.800	0.810	21.850	7.980
1 at.%	15.100	0.687	7.145	24.404
2 at.%	14.426	0.656	5.280	33.021
3 at.%	14.088	0.641	9.423	18.505
4 at.%	13.245	0.603	12.588	13.852
5 at.%	12.907	0.587	13.366	13.045

analyzed impedance data of the respective charge transfer resistance. *R* value relatively decreases with increasing Al dopant concentrations of 0 at.% to 2 at.%. This phenomenon can be attributed to the decreasing thickness of ATNs. A possible explanation for the decrease of *R* might be due to the shorter distance for the excitonic electrons under UV radiation to travel within the shorter length of the nanorods toward the FTO-coated glass for the sample with higher Al dopant concentration. Another possible explanation is the increase in conductivity caused by the substitution of Ti^{4+} by Al^{3+} in the rutile TiO_2 as described previously. The results of the low photocurrent at higher thickness are in line with those of previous studies [105,106].

However, the *R* value is gradually increased with decreasing thickness of the deposited ATNs as observed in the 3 at.% to 5 at.% samples. This result is therefore in line with the gradual decrease in the photocurrent to some extent. Thus, varying the Al dopant concentration results in the lowest value of *R* and highest value of photocurrent for 2 at.% of ATNs sample. This characteristic reflects that the optimum growth of ATNs maximizes the charge transfer process in the device under UV irradiation. Prior studies noted the importance of minimal value of *R* which is advantageous for high gain of photocurrent due to high electron mobility caused by the grain boundaries and nanoparticles of the TiO_2 nanostructure, low electron trapping, and low electron–hole recombination rate [84,103,104,107]. These results are in agreement with the measured photocurrent as described in previous studies which resulted in high performance of the fabricated UV photosensor. This phenomenon can be attributed to the low charge transfer resistance of the deposited ATNs. Hence, the investigation of charge transfer resistance shows that the total loss of photo-generated electrons during transportation determines the photocurrent gain and leads to the performance of the fabricated UV photosensor.

The Bode-phase plot of the fabricated UV photosensor using the deposited ATNs for the undoped and doped samples is shown in Fig. 12. The lifetime of electrons (τ) for the fabricated UV photosensor is analyzed from the maximum frequency of the peak from the Bode-phase plot based on the following equation [103]:

$$\tau = \frac{1}{2\pi f_{max}} \tag{14}$$

where f_{max} is the maximum frequency of the peak. The f_{max} values of the fabricated U*V* photosensor for the 0 at.% (undoped), 1 at.%, 2 at.%, 3 at.%, 4 at.%, and 5 at.% samples are 19.91, 6.51, 4.81, 8.59, 11.47, and 12.18 Hz, respectively.

Based on the f_{max}, the calculated τ can be described to rise from 7.98 to the maximum of 33.02 ms with increasing Al dopant concentrations

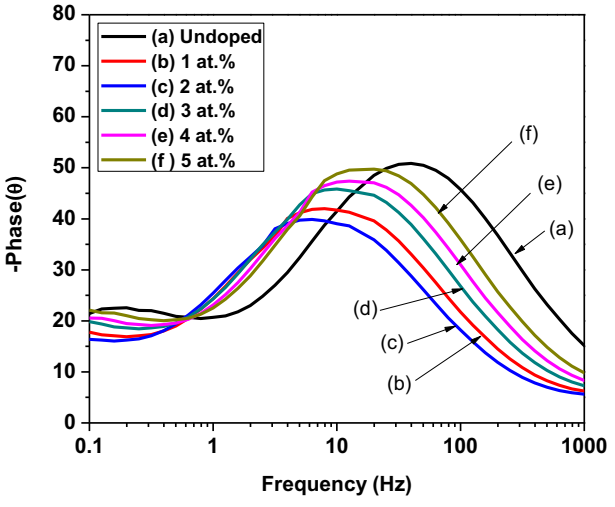

Fig. 12. EIS Bode phase plots under UV irradiation (365 nm, 750 μW/cm^2) of the fabricated UV photosensor using undoped TiO_2 and ATNs samples.

from 0 at.% to 2 at.% samples, respectively (Table 5). In general, high conductivity of ATNs as described in the I-V measurement increases the electron transportation to the back contact of the substrate to some extent. The decrease in *R* value attributed to the increase in conductivity as described earlier on the Nyquist plot also leads to the inhibition of electron–hole recombination throughout the ATNs/electrolyte interface. This phenomenon increases the generation of photocurrent. The analyzed τ value decreases to 18.51, 13.85, and 13.04 ms for the 3 at.%, 4 at.%, and 5 at.% samples, respectively. This result is congruent to those described in the earlier analysis on the photocurrent. Hence, the excess doping of Al concentration decreases the τ value, leading to the degradation of photocurrent caused by high recombination of excitonic charge carriers.

This phenomenon might be due to the fact that the diffusion of electrons in ATNs is subjected to the result of the photocurrent under UV irradiation. Although the length of ATNs increases the reactive surface area to detect UV irradiation, the diffusion of excitonic charge carriers is limited by the transportation between the boundaries of the nanostructures, which could hinder the moving pathway. This phenomenon increases the possibility of electron–hole recombination. The occurrence of electron–hole recombination is prone to the existence of electron-trapping mechanism at the boundary between the stacking of nanostructures [103,108,109]. Strong evidence of these explanations were found when the 2 at.% sample showed higher *I* (108.87 μA), lower *R* (5.28 kΩ), and higher τ (33.02 ms), compared with the other samples because of the high-quality reactive surface area and high electron mobility throughout the pathway toward the back contact of the substrate. Moreover, the doping of Al for all ATNs samples shows higher UV response through the measured photocurrent to some extent compared with the undoped sample.

4. Conclusion

In summary, ATNs were successfully grown on FTO-coated glass substrate using a facile single-step aqueous chemical growth in a modified Schott bottle at different Al doping concentrations. FESEM analysis showed that the length and diameter of the nanorod of the deposited ATNs decrease with increasing Al dopant concentrations. Structural analysis using XRD and Raman spectra showed that the deposited samples were crystalline rutile TiO_2. The fabricated UV photosensors with the deposited ATNs samples displayed outstanding performance by their stability under repeated switching and high response of photocurrent to rise and decay during the “on” and “off” states under UV irradiation at 0 V bias. The performance of the fabricated UV photosensor could be efficiently tuned by adjusting the Al dopant concentration during the growth of ATNs. The increased conductivity of the deposited ATNs increased the photocurrent to some extent due to the improved mobility of excitonic charge carriers under UV irradiation. However, the UV sensing performance for the synthesized samples started to decrease at higher Al dopant concentration because of the possible increase of electron-hole recombination. Thus, Al doping reduces the active surface area of ATNs/electrolyte interface, and the excess doping of Al concentration decreases the generated photocurrent. The best performance of the fabricated UV photosensor using the deposited ATNs was obtained from 2 at.% sample with measured photocurrent of 108.87 μA/cm. The fabricated UV photosensor based on the deposited ATNs structure could be used for practical applications in UV sensing devices because of its high performance, fast response and recovery, and simple and rapid fabrication process.

5. Acknowledgment

This work was supported by GIP grant (600-IRMI/MYRA 5/3/GIP (002/2017)). The authors would like to thank the Institute of Research Management and Innovation (IRMI) of UiTM and International Islamic University Malaysia (IIUM) for financial support.

References

[1] J. Ballester, T. García-Armingol, Diagnostic techniques for the monitoring and control of practical flames, Prog. Energy Combust. Sci. 36 (2010) 375–411.
[2] K.W. Liu, J.G. Ma, J.Y. Zhang, Y.M. Lu, D.Y. Jiang, B.H. Li, D.X. Zhao, Z.Z. Zhang, B. Yao, D.Z. Shen, Ultraviolet photoconductive detector with high visible rejection and fast photoresponse based on ZnO thin film, Solid State Electron. 51 (2007) 757–761.
[3] Y. Ngu, M.C. Peckerar, D. Sander, C.R. Eddy, M.A. Mastro, J.K. Hite, R.T. Holm, R.L. Henry, A. Tuchman, Array of two UV-wavelength detector types, IEEE Trans. Electron Devices 57 (2010) 1224–1229.
[4] H. Wang, Q. Sun, Y. Yao, Y. Li, J. Wang, L. Chen, A micro sensor based on TiO_2 nanorod arrays for the detection of oxygen at room temperature, Ceram. Int. 42 (2016) 8565–8571.
[5] A.M. Selman, Z. Hassan, M. Husham, N.M. Ahmed, A high-sensitivity, fast-response, rapid-recovery p–n heterojunction photodiode based on rutile TiO_2 nanorod array on p-Si(111), Appl. Surf. Sci. 305 (2014) 445–452.
[6] X. Yanru, W. Lin, L. Qinghao, C. Yanxue, Y. Shishen, J. Jun, L. Guolei, M. Liangmo, High-performance self-powered UV photodetectors based on TiO_2 nano-branched arrays, Nanotechnology 25 (2014) 075202.
[7] X. Zu, H. Wang, G. Yi, Z. Zhang, X. Jiang, J. Gong, H. Luo, Self-powered UV photodetector based on heterostructured TiO_2 nanowire arrays and polyaniline nanoflower arrays, Synth. Met. 200 (2015) 58–65.
[8] H.-y. Yang, X.-L. Cheng, X.-F. Zhang, Z.-k. Zheng, X.-f. Tang, Y.-M. Xu, S. Gao, H. Zhao, L.-H. Huo, A novel sensor for fast detection of triethylamine based on rutile TiO_2 nanorod arrays, Sensors Actuators B Chem. 205 (2014) 322–328.
[9] T. Ohno, T. Higo, N. Murakami, H. Saito, Q. Zhang, Y. Yang, T. Tsubota, Photocatalytic reduction of CO_2 over exposed-crystal-face-controlled TiO_2 nanorod having a brookite phase with co-catalyst loading, Appl. Catal. B Environ. 152–153 (2014) 309–316.
[10] F. Petronella, S. Diomede, E. Fanizza, G. Mascolo, T. Sibillano, A. Agostiano, M.L. Curri, R. Comparelli, Photodegradation of nalidixic acid assisted by TiO_2 nanorods/Ag nanoparticles based catalyst, Chemosphere 91 (2013) 941–947.
[11] C. Cao, C. Hu, X. Wang, S. Wang, Y. Tian, H. Zhang, UV sensor based on TiO2 nanorod arrays on FTO thin film, Sensors Actuators B Chem. 156 (2011) 114–119.
[12] O. Alev, E. Şennik, N. Kılınç, Z.Z. Öztürk, Gas sensor application of hydrothermally growth TiO_2 Nanorods, Proc. Eng. 120 (2015) 1162–1165.
[13] J. Lu, Z. Liu, C. Zhu, M. Zhang, M. Wan, Effect of the morphology of the TiO_2 nanorods on the photovoltaic properties of the dye-sensitized solar cells, Mater. Lett. 159 (2015) 61–63.
[14] M. Zhang, D. Li, J. Zhou, W. Chen, S. Ruan, Ultraviolet detector based on TiO_2 nanowire array–polymer hybrids with low dark current, J. Alloys Compd. 618 (2015) 233–235.
[15] A.M. Selman, Studies on the influence of growth time on the rutile TiO2 nanostructures prepared on Si substrates with fabricated high-sensitivity and fast-response p-n heterojunction photodiode, Am. J. Nano Res. Appl. 4 (2016) 23–32.
[16] A.M. Selman, Z. Hassan, Structural and photoluminescence studies of rutile TiO2 Nanorods prepared by CBD method on Si substrates, Am. J. Mater. Sci. 5 (2015) 16–20.
[17] M.R. Hoffmann, S.T. Martin, W. Choi, D.W. Bahnemann, Environmental applications of semiconductor Photocatalysis, Chem. Rev. 95 (1995) 69–96.
[18] W. Körner, C. Elsässer, Density functional theory study of dopants in polycrystalline TiO_2, Phys. Rev. B 83 (2011) 205315.
[19] I. Tsuyumoto, T. Hosono, M. Murata, Thermoelectric power in nonstoichiometric orthorhombic titanium oxides, J. Am. Ceram. Soc. 89 (2006) 2301–2303.
[20] T. Jinke, W. Wendong, Z. Guang-Lin, L. Qiang, Colossal positive Seebeck coefficient and low thermal conductivity in reduced TiO_2, J. Phys. Condens. Matter 21 (2009) 205703.
[21] H.A. Huy, B. Aradi, T. Frauenheim, P. Deák, Calculation of carrier-concentration-dependent effective mass in Nb-doped anatase crystals of TiO_2, Phys. Rev. B 83 (2011) 155201.
[22] T.-J. Ha, H.-H. Park, S.-Y. Jung, S.-J. Yoon, J.-S. Kim, H.W. Jang, Effect of porosity on the Seebeck coefficient of mesoporous TiO_2 thin films, Thin Solid Films 518 (2010) 7196–7198.
[23] E. Dy, R. Hui, J. Zhang, Z.-S. Liu, Z. Shi, Electronic conductivity and stability of doped Titania ($Ti_{1-X}M_XO_2$, M = Nb, Ru, and Ta)—a density functional theory-based comparison, J. Phys. Chem. C 114 (2010) 13162–13167.
[24] J. Nowotny, T. Bak, T. Burg, Electrical properties of polycrystalline TiO_2 thermoelectric power, Ionics 13 (2007) 155–162.
[25] S.-Y. Jung, T.-J. Ha, W.-S. Seo, Y.S. Lim, S. Shin, H.H. Cho, H.-H. Park, Thermoelectric properties of Nb-doped ordered mesoporous TiO_2, J. Electron. Mater. 40 (2011) 652–656.
[26] E. Palomares, J.N. Clifford, S.A. Haque, T. Lutz, J.R. Durrant, Control of charge recombination dynamics in dye sensitized solar cells by the use of Conformally deposited metal oxide blocking layers, J. Am. Chem. Soc. 125 (2003) 475–482.
[27] J.R. Durrant, S.A. Haque, E. Palomares, Towards optimisation of electron transfer processes in dye sensitised solar cells, Coord. Chem. Rev. 248 (2004) 1247–1257.
[28] H.J. Snaith, C. Ducati, SnO_2-based dye-sensitized hybrid solar cells exhibiting near Unity absorbed photon-to-Electron conversion efficiency, Nano Lett. 10 (2010) 1259–1265.
[29] S.G. Chen, S. Chappel, Y. Diamant, A. Zaban, Preparation of Nb_2O_5 coated TiO_2 Nanoporous electrodes and their application in dye-sensitized solar cells, Chem. Mater. 13 (2001) 4629–4634.
[30] T. Kirthi, B. Jayasundara, B. Priyangi Konara Mudiyanselage, K. Gamaralalage Rajanya Asoka, K. Akinori, Enhanced efficiency of a dye-sensitized solar cell made from MgO-coated Nanocrystalline SnO_2, Jpn. J. Appl. Phys. 40 (2001) L732.
[31] M. Wang, S. Plogmaker, R. Humphry-Baker, P. Pechy, H. Rensmo, S.M. Zakeeruddin, M. Grätzel, Molecular-scale Interface engineering of Nanocrystalline Titania by co-adsorbents for solar energy conversion, ChemSusChem 5 (2012) 181–187.
[32] Y. Lou, S. Yuan, Y. Zhao, P. Hu, Z. Wang, M. Zhang, L. Shi, D. Li, Molecular-scale interface engineering of metal nanoparticles for plasmon-enhanced dye sensitized solar cells, Dalton Trans. 42 (2013) 5330–5337.
[33] B.C. O'Regan, J.R. Durrant, P.M. Sommeling, N.J. Bakker, Influence of the $TiCl_4$ treatment on Nanocrystalline TiO_2 films in dye-sensitized solar cells. 2. Charge density, band edge shifts, and quantification of recombination losses at short circuit, J. Phys. Chem. C 111 (2007) 14001–14010.
[34] S. Murcia López, M.C. Hidalgo, J.A. Navío, G. Colón, Novel Bi_2WO_6–TiO_2 heterostructures for rhodamine B degradation under sunlike irradiation, J. Hazard. Mater. 185 (2011) 1425–1434.
[35] P. Zhou, J. Wu, W. Yu, G. Zhao, G. Fang, S. Cao, Vectorial doping-promoting charge transfer in anatase TiO_2 {001} surface, Appl. Surf. Sci. 319 (2014) 167–172.
[36] H. Feng, M.-H. Zhang, L.E. Yu, Hydrothermal synthesis and photocatalytic performance of metal-ions doped TiO_2, Appl. Catal. A Gen. 413–414 (2012) 238–244.
[37] C. Han, J. Andersen, V. Likodimos, P. Falaras, J. Linkugel, D.D. Dionysiou, The effect of solvent in the sol–gel synthesis of visible light-activated, sulfur-doped TiO_2 nanostructured porous films for water treatment, Catal. Today 224 (2014) 132–139.
[38] J. Yu, J. Xiong, B. Cheng, S. Liu, Fabrication and characterization of Ag–TiO_2 multiphase nanocomposite thin films with enhanced photocatalytic activity, Appl. Catal. B Environ. 60 (2005) 211–221.
[39] K. Das, S.N. Sharma, M. Kumar, S.K. De, Morphology dependent luminescence properties of Co doped TiO_2 nanostructures, J. Phys. Chem. C 113 (2009) 14783–14792.
[40] C. O'Rourke, D.R. Bowler, Intrinsic oxygen vacancy and extrinsic aluminum dopant interplay: a route to the restoration of defective TiO_2, J. Phys. Chem. C 118 (2014) 7261–7271.
[41] K. Manoharan, P. Venkatachalam, Photoelectrochemical performance of dye sensitized solar cells based on aluminum-doped titanium dioxide structures, Mater. Sci. Semicond. Process. 30 (2015) 208–217.
[42] A. Adamczyk, E. Długoń, The FTIR studies of gels and thin films of Al_2O_3–TiO_2 and Al_2O_3–TiO_2–SiO_2 systems, Spectrochim. Acta A Mol. Biomol. Spectrosc. 89 (2012) 11–17.
[43] S.-S. Lin, D.-K. Wu, Effect of RF deposition power on the properties of Al-doped TiO_2 thin films, Surf. Coat. Technol. 204 (2010) 2202–2207.
[44] D.J. Reidy, J.D. Holmes, M.A. Morris, The critical size mechanism for the anatase to rutile transformation in TiO_2 and doped-TiO_2, J. Eur. Ceram. Soc. 26 (2006) 1527–1534.
[45] K. Zhu, N.R. Neale, A. Miedaner, A.J. Frank, Enhanced charge-collection efficiencies and light scattering in dye-sensitized solar cells using oriented TiO2 nanotubes arrays, Nano Lett. 7 (2007) 69–74.
[46] L. Xu, M.P. Garrett, B. Hu, Doping effects on internally coupled Seebeck coefficient, electrical, and thermal conductivities in aluminum-doped TiO_2, J. Phys. Chem. C 116 (2012) 13020–13025.
[47] J.E. Lee, S.-M. Oh, D.-W. Park, Synthesis of nano-sized Al doped TiO_2 powders using thermal plasma, Thin Solid Films 457 (2004) 230–234.
[48] Y.S. Song, B.Y. Kim, N.I. Cho, D.Y. Lee, Effect of Al doping on optical band gap energy of Al-TiO_2 thin films, J. Nanosci. Nanotechnol. 15 (2015) 5228–5231.
[49] M.L. Taylor, G.E. Morris, R.S.C. Smart, Influence of aluminum doping on titania pigment structural and dispersion properties, J. Colloid Interface Sci. 262 (2003) 81–88.
[50] S.K. Kim, G.-J. Choi, S.Y. Lee, M. Seo, S.W. Lee, J.H. Han, H.-S. Ahn, S. Han, C.S. Hwang, Al-doped TiO_2 films with ultralow leakage currents for next generation DRAM capacitors, Adv. Mater. 20 (2008) 1429–1435.
[51] M. Rajabi, S. Shogh, A. Iraji zad, Defect study of TiO_2 nanorods grown by a hydrothermal method through photoluminescence spectroscopy, J. Lumin. 157 (2015) 235–242.
[52] X. Feng, K. Shankar, O.K. Varghese, M. Paulose, T.J. Latempa, C.A. Grimes, Vertically aligned single crystal TiO_2 nanowire arrays grown directly on transparent conducting oxide coated glass: synthesis details and applications, Nano Lett. 8 (2008) 3781–3786.
[53] T. Aguilar, J. Navas, R. Alcántara, C. Fernández-Lorenzo, J.J. Gallardo, G. Blanco, J. Martín-Calleja, A route for the synthesis of Cu-doped TiO_2 nanoparticles with a very low band gap, Chem. Phys. Lett. 571 (2013) 49–53.
[54] A.K. Tripathi, M.C. Mathpal, P. Kumar, M.K. Singh, M.A.G. Soler, A. Agarwal, Structural, optical and photoconductivity of Sn and Mn doped TiO_2 nanoparticles, J. Alloys Compd. 622 (2015) 37–47.
[55] D.M. de los Santos, J. Navas, A. Sánchez-Coronilla, R. Alcántara, C. Fernández-Lorenzo, J. Martín-Calleja, Highly Al-doped TiO_2 nanoparticles produced by ball mill method: structural and electronic characterization, Mater. Res. Bull. 70 (2015) 704–711.
[56] W. Zhang, X. Pei, J. Chen, H. He, Effects of Al doping on properties of xAl–3% In–TiO_2 photocatalyst prepared by a sol–gel method, Mater. Sci. Semicond. Process. 38 (2015) 24–30.
[57] J. Wu, S. Lo, K. Song, B.K. Vijayan, W. Li, K.A. Gray, V.P. Dravid, Growth of rutile TiO_2 nanorods on anatase TiO_2 thin films on Si-based substrates, J. Mater. Res. 26 (2011) 1646–1652.
[58] H. Cheng, J. Ma, Z. Zhao, L. Qi, Hydrothermal preparation of uniform Nanosize rutile and Anatase particles, Chem. Mater. 7 (1995) 663–671.
[59] B. Liu, E.S. Aydil, Growth of oriented single-crystalline rutile TiO_2 Nanorods on

transparent conducting substrates for dye-sensitized solar cells, J. Am. Chem. Soc. 131 (2009) 3985–3990.
[60] V. Etacheri, M.K. Seery, S.J. Hinder, S.C. Pillai, Oxygen rich Titania: a dopant free, high temperature stable, and visible-light active Anatase Photocatalyst, Adv. Funct. Mater. 21 (2011) 3744–3752.
[61] Y. Shao, D. Tang, J. Sun, Y. Lee, W. Xiong, Lattice deformation and phase transformation from nano-scale anatase to nano-scale rutile TiO_2 prepared by a sol-gel technique, China Particuology 2 (2004) 119–123.
[62] A.M. Selman, Z. Hassan, Growth and characterization of rutile TiO2 nanorods on various substrates with fabricated fast-response metal–semiconductor–metal UV detector based on Si substrate, Superlattice. Microst. 83 (2015) 549–564.
[63] K.R. Nemade, R.V. Barde, S.A. Waghuley, Liquefied petroleum gas sensing by Al-doped TiO_2 nanoparticles synthesized by chemical and solid-state diffusion routes, J. Taibah Univ. Sci. 10 (2016) 345–351.
[64] M.F. Malek, M.H. Mamat, Z. Khusaimi, M.Z. Sahdan, M.Z. Musa, A.R. Zainun, A.B. Suriani, N.D. Md Sin, S.B. Abd Hamid, M. Rusop, Sonicated sol–gel preparation of nanoparticulate ZnO thin films with various deposition speeds: the highly preferred c-axis (002) orientation enhances the final properties, J. Alloys Compd. 582 (2014) 12–21.
[65] L. Filipovic, S. Selberherr, Performance and stress analysis of metal oxide films for CMOS-integrated gas sensors, Sensors 15 (2015) 7206.
[66] H.A. Macleod, Thin-film Optical Filters, Macmillan Publishing Company, 1986.
[67] S.-S. Lin, D.-K. Wu, The properties of Al-doped TiO_2 nanoceramic films deposited by simultaneous rf and dc magnetron sputtering, Ceram. Int. 36 (2010) 87–91.
[68] L. Miao, S. Tanemura, Y. Kondo, M. Iwata, S. Toh, K. Kaneko, Microstructure and bactericidal ability of photocatalytic TiO_2 thin films prepared by rf helicon magnetron sputtering, Appl. Surf. Sci. 238 (2004) 125–131.
[69] M. Ye, D. Zheng, M. Lv, C. Chen, C. Lin, Z. Lin, Hierarchically structured nanotubes for highly efficient dye-sensitized solar cells, Adv. Mater. 25 (2013) 3039–3044.
[70] F. Shao, J. Sun, L. Gao, S. Yang, J. Luo, Forest-like TiO_2 hierarchical structures for efficient dye-sensitized solar cells, J. Mater. Chem. 22 (2012) 6824–6830.
[71] M.J. Alam, D.C. Cameron, Preparation and properties of transparent conductive aluminum-doped zinc oxide thin films by sol–gel process, J. Vac. Sci. Technol. A 19 (2001) 1642–1646.
[72] M. Zhang, M. Zhang, S. Shi, X. Song, Z. Sun, An approach toward TiO_2 nanostructure growth with tunable properties: influence of reaction time in a hydrothermal process, J. Alloys Compd. 591 (2014) 213–217.
[73] P. Jain, P. Arun, Influence of grain size on the band-gap of annealed SnS thin films, Thin Solid Films 548 (2013) 241–246.
[74] X. Shen, J. Zhang, B. Tian, Microemulsion-mediated solvothermal synthesis and photocatalytic properties of crystalline titania with controllable phases of anatase and rutile, J. Hazard. Mater. 192 (2011) 651–657.
[75] Q. Gao, X. Wu, Y. Fan, X. Zhou, Low temperature synthesis and characterization of rutile TiO_2-coated mica–titania pigments, Dyes Pigments 95 (2012) 534–539.
[76] S.-M. Oh, T. Ishigaki, Preparation of pure rutile and anatase TiO_2 nanopowders using RF thermal plasma, Thin Solid Films 457 (2004) 186–191.
[77] V. Swamy, Size-dependent modifications of the first-order Raman spectra of nanostructured rutile TiO_2, Phys. Rev. B 77 (2008) 195414.
[78] D. Wang, J. Zhao, B. Chen, C. Zhu, Lattice vibration fundamentals in nanocrystalline anatase investigated with Raman scattering, J. Phys. Condens. Matter 20 (2008) 085212.
[79] M.I. Zaki, A. Katrib, A.I. Muftah, T.C. Jagadale, M. Ikram, S.B. Ogale, Exploring anatase-TiO_2 doped dilutely with transition metal ions as nano-catalyst for H_2O_2 decomposition: spectroscopic and kinetic studies, Appl. Catal. A Gen. 452 (2013) 214–221.
[80] W. Alamgir, S. Khan, M. Ahmad, A.H. Naqvi Mehedi Hassan, Structural phase analysis, band gap tuning and fluorescence properties of Co doped TiO_2 nanoparticles, Opt. Mater. 38 (2014) 278–285.
[81] M. Kang, The superhydrophilicity of Al–TiO_2 nanometer sized material synthesized using a solvothermal method, Mater. Lett. 59 (2005) 3122–3127.
[82] S. Liu, G. Liu, Q. Feng, Al-doped TiO_2 mesoporous materials: synthesis and photodegradation properties, J. Porous. Mater. 17 (2010) 197–206.
[83] W.F. Zhang, Y.L. He, M.S. Zhang, Z. Yin, Q. Chen, Raman scattering study on anatase TiO_2 nanocrystals, J. Phys. D. Appl. Phys. 33 (2000) 912.
[84] S.S. Mali, C.S. Shim, H. Kim, C.K. Hong, Single step synthesized 1D TiO_2 vertically aligned nanorod arrays for CdS sensitized quantum dot sensitized solar cells, Ceram. Int. 42 ((2016) 1973–1981.
[85] N.J. Kim, Y.H. La, S.H. Im, B.K. Ryu, Optical and structural properties of Fe–TiO_2 thin films prepared by sol–gel dip coating, Thin Solid Films 518 (2010) 156–160.
[86] S. Sadhu, P. Poddar, Template-free fabrication of highly-oriented single-crystalline 1D-rutile TiO_2-MWCNT composite for enhanced Photoelectrochemical activity, J. Phys. Chem. C 118 (2014) 19363–19373.
[87] S. Batakrushna, P.K. Giri, I. Kenji, F. Minoru, Microscopic origin of lattice contraction and expansion in undoped rutile TiO_2 nanostructures, J. Phys. D. Appl. Phys. 47 (2014) 215302.
[88] S. Savaş, A. Aysun, S. Tülay, S. Necmi, The effects of film thickness on the optical properties of TiO_2–SnO_2 compound thin films, Phys. Scr. 84 (2011) 065602.
[89] M. Landmann, E. Rauls, W.G. Schmidt, The electronic structure and optical response of rutile, anatase and brookite TiO_2, J. Phys. Condens. Matter 24 (2012) 195503.
[90] J. Zhang, P. Zhou, J. Liu, J. Yu, New understanding of the difference of photocatalytic activity among anatase, rutile and brookite TiO_2, Phys. Chem. Chem. Phys. 16 (2014) 20382–20386.
[91] R. Wang, K. Hashimoto, A. Fujishima, M. Chikuni, E. Kojima, A. Kitamura, M. Shimohigoshi, T. Watanabe, Photogeneration of highly amphiphilic TiO_2 surfaces, Adv. Mater. 10 (1998) 135–138.
[92] M. Miyauchi, N. Kieda, S. Hishita, T. Mitsuhashi, A. Nakajima, T. Watanabe, K. Hashimoto, Reversible wettability control of TiO_2 surface by light irradiation, Surf. Sci. 511 (2002) 401–407.
[93] K. Hatta, M. Higuchi, J. Takahashi, K. Kodaira, Floating zone growth and characterization of aluminum-doped rutile single crystals, J. Cryst. Growth 163 (1996) 279–284.
[94] L. Zhou, L. Wei, Y. Yang, X. Xia, P. Wang, J. Yu, T. Luan, Improved performance of dye sensitized solar cells using cu-doped TiO_2 as photoanode materials: band edge movement study by spectroelectrochemistry, Chem. Phys. 475 (2016) 1–8.
[95] P. Su, H. Li, J. Wang, J. Wu, B. Zhao, F. Wang, Facile preparation of titanium dioxide nano-capsule arrays used as photo-anode for dye sensitized solar cells, Appl. Surf. Sci. 347 (2015) 636–642.
[96] M. Razeghi, A. Rogalski, Semiconductor ultraviolet detectors, J. Appl. Phys. 79 (1996) 7433.
[97] M. Okuya, K. Shiozaki, N. Horikawa, T. Kosugi, G.R.A. Kumara, J. Madarász, S. Kaneko, G. Pokol, Porous TiO_2 thin films prepared by spray pyrolysis deposition (SPD) technique and their application to UV sensors, Solid State Ionics 172 (2004) 527–531.
[98] L. Zhang, E. Reisner, J.J. Baumberg, Al-doped ZnO inverse opal networks as efficient electron collectors in $BiVO_4$ photoanodes for solar water oxidation, Energy Environ. Sci. 7 (2014) 1402–1408.
[99] K. Park, K.Y. Ko, Effect of TiO_2 on high-temperature thermoelectric properties of ZnO, J. Alloys Compd. 430 (2007) 200–204.
[100] T. Zhai, L. Li, X. Wang, X. Fang, Y. Bando, D. Golberg, Recent developments in one-dimensional inorganic nanostructures for photodetectors, Adv. Funct. Mater. 20 (2010) 4233–4248.
[101] J.D. Prades, F. Hernandez-Ramirez, R. Jimenez-Diaz, M. Manzanares, T. Andreu, A. Cirera, A. Romano-Rodriguez, J.R. Morante, The effects of electron–hole separation on the photoconductivity of individual metal oxide nanowires, Nanotechnology 19 (2008) 465501.
[102] X. Li, C. Gao, H. Duan, B. Lu, X. Pan, E. Xie, Nanocrystalline TiO_2 film based photoelectrochemical cell as self-powered UV-photodetector, Nano Energy 1 (2012) 640–645.
[103] P. Zhao, S. Yao, M. Wang, B. Wang, P. Sun, F. Liu, X. Liang, Y. Sun, G. Lu, High-efficiency dye-sensitized solar cells with hierarchical structures titanium dioxide to transfer photogenerated charge, Electrochim. Acta 170 (2015) 276–283.
[104] P.B. Patil, S.S. Mali, V.V. Kondalkar, K.V. Khot, R.M. Mane, C.K. Hong, P.S. Patil, J.H. Kim, P.N. Bhosale, An approach towards TiO_2 chrysanthemum flowers with tunable properties: influence of reaction time in hydrothermal process, J. Mater. Sci. Mater. Electron. 26 (2015) 6119–6128.
[105] A. Mathew, G.M. Rao, N. Munichandraiah, Effect of TiO_2 electrode thickness on photovoltaic properties of dye sensitized solar cell based on randomly oriented Titania nanotubes, Mater. Chem. Phys. 127 (2011) 95–101.
[106] C.-P. Hsu, K.-M. Lee, J.T.-W. Huang, C.-Y. Lin, C.-H. Lee, L.-P. Wang, S.-Y. Tsai, K.-C. Ho, EIS analysis on low temperature fabrication of TiO_2 porous films for dye-sensitized solar cells, Electrochim. Acta 53 (2008) 7514–7522.
[107] M. Zhu, L. Chen, H. Gong, M. Zi, B. Cao, A novel TiO_2 nanorod/nanoparticle composite architecture to improve the performance of dye-sensitized solar cells, Ceram. Int. 40 ((2014) 2337–2342.
[108] J. Bisquert, F. Fabregat-Santiago, I. Mora-Seró, G. Garcia-Belmonte, S. Giménez, Electron lifetime in dye-sensitized solar cells: theory and interpretation of measurements, J. Phys. Chem. C 113 (2009) 17278–17290.
[109] P. Qiang, Z. Chen, P. Yang, X. Cai, S. Tan, P. Liu, W. Mai, TiO_2 nanowires for potential facile integration of solar cells and electrochromic devices, Nanotechnology 24 (2013) 435403.